Computer Fraud and Security
ISSN (online): 1873-7056

Research and Evaluation Analysis of Sliding Mode Control based on Linear Matrix Inequality for Two-Wheeled Self-Balancing Robot

Huaqiang Zhang, Norzalilah Mohamad Nor*

Department of Mechanical Engineering, Faculty of Engineering, Universiti Sains Malaysia, Jln Transkrian - Bukit Panchor, 14300 Nibong Tebal, Pulau Pinang, Malaysia

**Corresponding Author's Email: norzalilah@usm.my*

Abstract: The dynamic model of a two-wheeled self-balancing robot (TWSBR) has the characteristics of multivariable, strong coupling, nonlinear, and unstable control performance. In this paper, the mathematical model of the motor is combined with the Lagrangian equation of motion, and the dynamic model of the TWSBR based on voltage as the control input is re-established. Based on this dynamic model, a novel sliding mode control method based on linear matrix inequality (LMI-SMC) optimization is designed. The stability of TWSBR is proved using Lyapunov's theorem. Finally, the sliding mode control method and the stability of TWSBR are verified through simulation. A detailed comparison with other typical control methods is carried out. The simulation results show that the sliding mode controller reduces the steady-state error, suppresses the chatting, and is robust.

Keywords: two-wheeled self-balancing robot; linear matrix inequality; sliding mode control; Lyapunov's proof; Comprehensive weighted performance evaluation index.

1. Introduction

TWSBR is a particular type of robot, usually consisting of two wheels and some sensors that can adjust to maintain a balanced state[1]. The advantages of TWSBR are mainly reflected in their flexibility, self-balancing ability, efficient energy utilization, and versatility[2]. The robot can move flexibly in a small space, balance itself without external support, and use energy efficiently, making it suitable for various application scenarios[3]. In addition, TWSBR has good human-computer interaction and technological attraction, can interact with humans, and has attracted attention in scientific research, education, and enterprises[4]. This kind of robot has potential application value in improving production efficiency, reducing labor costs, and improving the working environment[5].

As a statically unstable system, the first problem to be solved for a TWSBR is balance control[6]. To achieve this, researchers generally need to establish a dynamic model of the robot, which can be designed based on Newtonian mechanics, Lagrangian mechanics, and Kane modeling methods[7].

The Newton-Euler method uses Newtonian mechanics to analyze the robot's force and obtains the dynamic model through simultaneous equations. Although this method is cumbersome and error-prone, it is relatively intuitive, so most researchers use it to model robots. The Newton-Euler method was employed by E. H. Karam et al.[8] for modeling a TWSBR. They designed a robust controller for controlling TWSBR with a state-feedback-based sliding mode controller (SFSMC) to solve the balancing and tracking problems. The Newton-Euler method was utilized by V. Mudeng et al.[9] to model a TWSBR and maintain it in equilibrium. The authors applied a proportional-integral differential (PID) controller as a control system for a TWSBR and achieved good results. The Lagrangian function method analyzes from the energy point of view, avoids the complicated analysis of internal forces, and can effectively simplify the modeling process. The robot equations of motion are derived using the Lagrangian and mapped to transfer functions in the complex s-domain in [10]. The control is implemented on an Arduino microcontroller using a zero-order hold discretization method. C. Iwendi et al.[11] used Lagrangian equations and developed a robot model. This study conducted experiments on the PD-PI

navigation control of TWSBR to achieve maximum obstacle avoidance. The Kane method also starts from the generalized coordinates without considering the internal forces of the system, and the Kane method is the most excellent model method proposed recently. The Kane method was employed by H. Ahmadi Jeyed et al.[12] to derive a three-degree-of-freedom (3-DOF) model of a TWSBR, encompassing the longitudinal displacement, yaw, and pitch motion of the chassis.

The controller design and stability proofs are based on precise mathematical models without any uncertainties taken into account. However, uncertainties and model mismatches between nominal mathematical models and actual plants are inevitable. Sliding mode control is robust and can effectively suppress system parameter uncertainties and external disturbances. A study of sliding mode control in a TWSBR is presented in [13]. They designed a full-state feedback controller (LQR) and a sliding mode controller. Simulations show that the sliding mode controller outperforms full-state feedback control in controlling a TWSBR. A robust sliding mode controller is proposed in [15] for tracking a TWSBR under terrain inclination and disturbances. The controller is designed using a continuous approximation around the switch surface to minimize chattering phenomena. In [14], the dynamic equations of the system are given, and two control methods, cascade control, and sliding mode control, are applied to the system. Two control methods for stabilizing a TWSBR are investigated in [16]. A mathematical kinetic model is constructed using the Lagrangian function method. A sliding mode controller (SMC) for automatic balance and yaw rotation is proposed. Experimental results show that the SMC controller outperforms (LQR) in transient performance and noise immunity. Developing a robust sliding mode-based controller for a TWSBR is discussed in [17]. Control can be smoothed by approximating discontinuous functions to continuous functions.

The combination of sliding mode control and other control methods has apparent advantages in controlling TWSBR. Sliding mode control provides stable control of the system through its robustness and fast response. Other control methods, such as PID control[18–20], LQR control[21–23], fuzzy control[24–27], neural network control[28– 31], Sliding mode control[32–34], adaptive control[35–37], Optional control[38, 39], and Artificial intelligence[40–42], can further optimize the controller's performance and deal with problems such as inaccurate modeling and unknown system parameters. Research on hybrid control methods can improve the performance and stability of TWSBR under different working conditions. However, in-depth theoretical analysis and experimental verification are needed to determine the optimal control strategy and parameter settings.

Linear matrix inequalities (LMI) have significant advantages in control theory. LMI is a robust analysis and design tool that can be used for system stability analysis, performance optimization, and other issues. In addition, the LMI method is easy to calculate and implement, can be solved by convex optimization technology, and has the characteristics of scalability and broad applicability. The performance of observer-based LQR and LMI controllers for the vertical stability control of a nonlinear TWSBR is investigated in [43]. A robust attitude controller is proposed in [44] for TWSBR to enhance stability during ramp driving by maintaining a balanced body attitude angle and wheel angular velocity target values. This paper uses LMI to design a feedback system controller that meets performance requirements and compensates for impulsive disturbance robustness through state feedback. A dual-loop robust control design method is proposed in [45], which consists of two degrees of freedom to coordinate nominal and robust performance, respectively. LMI solvability conditions are used to synthesize full-order H_2/H_∞ controls.

The main contributions of this paper are summarized as follows:

1. The motor model is added to TWSBR, and the overall mathematical model, whose input is voltage, is redesigned.

2. A novel sliding mode control based on linear matrix inequality (LMI-SMC) was designed, and the stability of the control method was proven using the Lyapunov method.

3. The performance of LMI-SMC with other typical optimal controllers is compared under various working conditions.

4. A novel comprehensive weighted performance evaluation index (CWPEI) is proposed to evaluate control performance under the same conditions more fairly.

The rest of this paper is organized as follows. Section II establishes a dynamic model of TWSBR based on controlling the motor voltage. In Section III, an LMISMC controller is designed. In Section IV, the controller's performance is simulated, and the evaluation criteria for the performance of TWSBR are redesigned. Meanwhile, its performance is compared with other typical optimization controllers. In Section V, an experimental study is conducted, and TWSBR is verified in a 3D simulation environment. The simulation proves that the controller in this paper has good control performance. In Section VI, this paper is summarized and concluded.

2. Methodology

2.1. Preliminary

The design of the TWSBR is shown in Fig.1(a). The mechanical mechanism of TWSBR mainly includes an inverted pendulum mounted on a pair of wheels, each wheel driven by an independent motor. The dynamics of a TWSBR is an underactuated system with only two inputs but three degrees of freedom. Due to the unique physics of such robotic systems, we can decouple the overall dynamics of the vehicle into two decoupled subsystems.

The first subsystem consists of the first equation of robot dynamics, called the ϕ subsystem, with $u_2 = v_l - v_r$ as the control input, also known as the steering subsystem. The second subsystem consists of the last two equations of vehicle dynamics, called the $\{\theta, \psi\}$ subsystem, with $u_1 = v_l + v_r$ as the control input, also known as a self-balancing subsystem, where the driver is insufficient. Considering variable structure technology's parameter insensitivity and anti-interference characteristics, this paper uses the sliding mode control method to design the control inputs u_1 an u_2.

In particular, we assume that $\phi_d(t), \psi_d(t)$ and $\theta_d(t)$ are bounded and twice continuously differentiable. In general terms, the requirements of $\phi_d(t)$ and $\theta_d(t)$ are guaranteed. As for $\psi_d(t)$, as mentioned before, it is determined by robot dynamics and rolling friction resistance. According to practical experience, if the high-order dynamics of the robot are ignored, the necessary conditions of $\psi_d(t)$ (boundedness and quadratic continuous differentiability) can also be satisfied. Such control target research can achieve the goal.

Fig.1(b) shows a side view of the TWSBR. The coordinate system used in 2 Motion Equations of TWSBR is described in Fig.1(c). The physical parameters of the TWSBR are shown in Tab 1. R_M, K_b, and K_t values are extracted from [46], whereas the values for J_m, n, f_m, f_W, and few are selected appropriately since they are hard to measure.

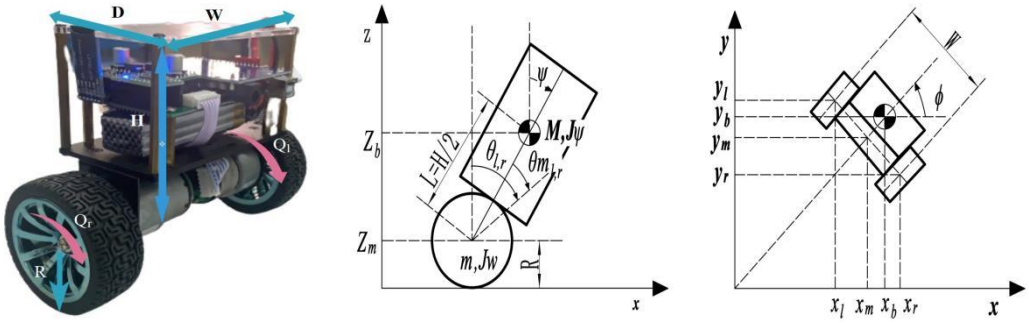

(a) TWSBR (b) Side view of TWSBR (c) Plane view of TWSBR

Figure 1. TWSBR

2.2. Motion Equations of TWSBR

According to the coordinate systems in Fig.1(b) and Fig.1(c), the motion equation of TWSBR can be derived using the Lagrangian method. If the motion direction of TWSBR at time $t = 0$ is the positive direction of the x-axis, then the coordinates are as follows.

$$(\theta,\phi)=\left(\frac{1}{2}(\theta_l+\theta_r),\frac{R}{W}(\theta_r-\theta_l)\right) \tag{1}$$

$$(x_m,y_m,z_m)=\left(\int \dot{x}_m dt,\int \dot{y}_m dt,R\right) \tag{2}$$

$$(\dot{x}_m,\dot{y}_m)=\left(R\dot{\theta}\cos\phi,R\dot{\theta}\sin\phi\right) \tag{3}$$

$$(x_l,y_l,z_l)=\left(x_m-\frac{W}{2}\sin\phi,y_m+\frac{W}{2}\cos\phi,z_m\right) \tag{4}$$

$$(x_r,y_r,z_r)=\left(x_m+\frac{W}{2}\sin\phi,y_m-\frac{W}{2}\cos\phi,z_m\right) \tag{5}$$

$$(x_b,y_b,z_b)=(x_m+L\sin\psi\cos\phi,y_m+L\sin\psi\sin\phi,z_m+L\cos\psi) \tag{6}$$

Table 1. Robot parameters

Robot Parameters	Interpretation
$g=9.81\text{m/s}^2$	Gravity acceleration
$m=0.051\text{kg}$	Wheel weight
$R=0.0325\text{m}$	Wheel radius
$J_W=\frac{mR^2}{2}\text{kg}\cdot\text{m}^2$	Wheel inertia moment
$M=0.703\text{kg}$	Body weight
$W=0.192\text{m}$	Body width
$D=0.082\text{m}$	Body depth
$H=0.112\text{m}$	Body height
$L=\frac{H}{2}\text{m}$	Distance of the center of mass from the wheel axle
$J_\psi=\frac{ML^2}{3}\text{kg}\cdot\text{m}^2$	Body pitch inertia moment

$J_\phi = \frac{M(W^2 + D^2)}{12} \mathrm{kg \cdot m^2}$	Body yaw inertia moment
$J_m = 1 \times 10^{-5} \mathrm{kg \cdot m^2}$	DC motor inertia moment
$R_m = 2.9\Omega$	DC motor resistance
$K_b = 0.024 \mathrm{V \cdot s/rad}$	DC motor back EMF constant
$K_t = 0.025 \mathrm{N \cdot m/A}$	DC motor torque constant
$n = 30$	Gear ratio
$f_m = 0.0022$	Friction coefficient between body and DC motor
$f_W = 0$	Friction coefficient between wheel and floor

Where ψ represents the body pitch angle, $\theta_{l,r}$ represents the wheel angle (l, r represents the left wheel and right wheel), $\theta_{m_{l,r}}$ represents the DC motor Angle, (x_m, y_m, z_m) represents the coordinate value of the center position of TWSBR, (x_l, y_l, z_l)represents the coordinate value of the left wheel position, (x_r, y_r, z_r) represents the coordinate value of the right wheel position.(x_b, y_b, z_b) represents the coordinate value of the center of gravity of TWSBR.

The translational energy T_1, rotational kinetic energy T_2, and potential energy U are as follows:

$$T_1 = \frac{1}{2}m\left(\dot{x}_l^2 + \dot{y}_l^2 + \dot{z}_l^2\right) + \frac{1}{2}m\left(\dot{x}_r^2 + \dot{y}_r^2 + \dot{z}_r^2\right) + \frac{1}{2}M\left(\dot{x}_b^2 + \dot{y}_b^2 + \dot{z}_b^2\right) \tag{7}$$

$$T_2 = \frac{1}{2}J_w\dot{\theta}_l^2 + \frac{1}{2}J_w\dot{\theta}_r^2 + \frac{1}{2}J_\psi\dot{\psi}^2 + \frac{1}{2}J_\phi\dot{\phi}^2 + \frac{1}{2}n^2J_m\left(\dot{\theta}_l - \dot{\psi}\right)^2 + \frac{1}{2}n^2J_m\left(\dot{\theta}_r - \dot{\psi}\right)^2 \tag{8}$$

$$U = mgz_l + mgz_r + Mgz_b \tag{9}$$

The fifth and sixth terms in T_2 are the rotation kinetic energy of an armature in the left and right DC motor. The Lagrangian L has the following expression.

$$L = T_1 + T_2 + U \tag{10}$$

The following variables are used as generalized coordinates: θ: Average angle of left and right wheel , ψ : Body pitch angle, ϕ : Body yaw angle. Following are the Lagrange equations:

$$\frac{d}{dt}\left(\frac{\partial L}{\partial \dot{\theta}}\right) - \frac{\partial L}{\partial \theta} = F_\theta \tag{11}$$

$$\frac{d}{dt}\left(\frac{\partial L}{\partial \dot{\psi}}\right) - \frac{\partial L}{\partial \psi} = F_\psi \tag{12}$$

$$\frac{d}{dt}\left(\frac{\partial L}{\partial \dot{\phi}}\right)-\frac{\partial L}{\partial \phi}=F_{\phi} \tag{13}$$

The following equation is derived by evaluating equations (11), (12) and (13).

$$\left[(2m+M)R^2+2J_w+2n^2J_m\right]\ddot{\theta}+\left(MLR\cos\psi-2n^2J_m\right)\ddot{\psi}-MLR\dot{\psi}^2\sin\psi=F_{\theta} \tag{14}$$

$$\begin{aligned}&\left(MLR\cos\psi-2n^2J_m\right)\ddot{\theta}+\left(ML^2+J_{\psi}+2n^2J_m\right)\ddot{\psi}\\&-MgL\sin\psi-ML^2\dot{\phi}^2\sin\psi\cos\psi=F_{\psi}\end{aligned} \tag{15}$$

$$\left[\frac{1}{2}mW^2+J_{\phi}+\frac{W^2}{2R^2}\left(J_w+n^2J_m\right)+ML^2\sin^2\psi\right]\ddot{\phi}+2ML^2\dot{\psi}\dot{\phi}\sin\psi\cos\psi=F_{\phi} \tag{16}$$

In consideration of DC motor torque and viscous friction, the generalized forces are given as the following:

$$\left(F_{\theta},\quad F_{\psi},\quad F_{\phi}\right)=\left(F_l+F_r,\quad F_{\psi},\quad \frac{W}{2R}\left(F_r-F_l\right)\right) \tag{17}$$

$$F_l=nK_ti_l+f_m\left(\dot{\psi}-\dot{\theta}_l\right)-f_w\dot{\theta}_l \tag{18}$$

$$F_r=nK_ti_r+f_m\left(\dot{\psi}-\dot{\theta}_r\right)-f_w\dot{\theta}_r \tag{19}$$

$$F_{\psi}=-nK_ti_l-nK_ti_r-f_m\left(\dot{\psi}-\dot{\theta}_l\right)-f_m\left(\dot{\psi}-\dot{\theta}_r\right) \tag{20}$$

Where $i_{l,r}$ is the DC motor current.

A DC motor cannot be controlled directly by current, as it is PWM (voltage) based. Therefore, we use the DC motor equations to evaluate the current $i_{l,r}$ and the voltage $v_{l,r}$. If the friction inside the motor is negligible, the DC motor equations are usually as follows:

$$L_m\dot{i}_{l,r}=v_{l,r}+K_b\left(\dot{\psi}-\dot{\theta}_{l,r}\right)-R_mi_{l,r} \tag{21}$$

Here, it is assumed that the motor inductance can be ignored at approximately zero. Therefore, the current is

$$i_{l,r}=\frac{v_{l,r}+K_b\left(\dot{\psi}-\dot{\theta}_{l,r}\right)}{R_m} \tag{22}$$

The generalized force can be expressed using the motor voltage.

$$F_{\theta}=\alpha\left(v_l+v_r\right)-2\left(\beta+f_w\right)\dot{\theta}+2\beta\dot{\psi} \tag{23}$$

$$F_{\psi}=-\alpha\left(v_l+v_r\right)+2\beta\dot{\theta}-2\beta\dot{\psi} \tag{24}$$

$$F_{\phi}=\frac{W}{2R}\alpha\left(v_r-v_l\right)-\frac{W^2}{2R^2}\left(\beta+f_w\right)\dot{\phi} \tag{25}$$

$$\alpha = \frac{nK_t}{R_m}, \quad \beta = \frac{nK_tK_b}{R_m} + f_m \tag{26}$$

2.3. State Equations of TWSBR

The state equations are derived based on modern control theory by linearizing the equations of motion of the equilibrium point of TWSBR. Considering the limit $\psi \to 0(\sin\psi \to \psi, \cos\psi \to 1)$ and ignoring the second-order terms such as $\dot{\psi}^2$, the equations of motion (14)-(16) are approximated as follows:

$$[(2m+M)R^2 + 2J_w + 2n^2J_m]\ddot{\theta} + \left(MLR - 2n^2J_m\right)\ddot{\psi} = F_\theta \tag{27}$$

$$\left(MLR - 2n^2J_m\right)\ddot{\theta} + \left(ML^2 + J_\psi + 2n^2J_m\right)\ddot{\psi} - MgL\psi = F_\psi \tag{28}$$

$$\left[\frac{1}{2}mW^2 + J_\phi + \frac{W^2}{2R^2}\left(J_w + n^2J_m\right)\right]\ddot{\phi} = F_\phi \tag{29}$$

Eqs. (27) and (28) have θ, and ψ, Eq. (29) has ϕ only. Eqs. (27) and (28) can be expressed in the form:

$$E\begin{bmatrix}\ddot{\theta}\\ \ddot{\psi}\end{bmatrix} + F\begin{bmatrix}\dot{\theta}\\ \dot{\psi}\end{bmatrix} + G\begin{bmatrix}\theta\\ \psi\end{bmatrix} = H\begin{bmatrix}v_l\\ v_r\end{bmatrix} \tag{30}$$

E, F, G ,and H in (30)

$$E = \begin{bmatrix} (2m+M)R^2 + 2J_w & MLR \\ +2n^2J_m & -2n^2J_m \\ \\ MLR - 2n^2J_m & ML^2 + J_\psi + 2n^2J_m \end{bmatrix}$$

$$F = 2\begin{bmatrix}\beta + f_w & -\beta \\ -\beta & \beta\end{bmatrix}, G = \begin{bmatrix}0 & 0 \\ 0 & -MgL\end{bmatrix}, H = \begin{bmatrix}\alpha & \alpha \\ -\alpha & -\alpha\end{bmatrix}$$

Eq. (29) can be expressed in the form:

$$I\ddot{\phi} + J\dot{\phi} = K\left(v_r - v_l\right) \tag{31}$$

I, J and K in (31)

$$I = \frac{1}{2}mW^2 + J_\phi + \frac{W^2}{2R^2}\left(J_w + n^2J_m\right), J = \frac{W^2}{2R^2}\left(\beta + f_w\right), K = \frac{W}{2R}\alpha$$

Consider the following variables x_1, x_2 as states and u as input. x^T represents the transpose of x.

$$\mathbf{x}_1 = \left[\theta, \quad \psi, \quad \dot{\theta}, \quad \dot{\psi}\right]^T, \mathbf{x}_2 = \left[\phi, \quad \dot{\phi}\right]^T, \mathbf{u} = \left[v_l, \quad v_r\right]^T$$

Therefore, the state equation of the TWSBR is derived from Eq. (30) and Eq. (31).

$$\dot{\mathbf{x}}_1 = A_1\mathbf{x}_1 + B_1\mathbf{u} \tag{32}$$

$$\dot{\mathbf{x}}_2 = A_2\mathbf{x}_2 + B_2\mathbf{u} \tag{33}$$

The matrix A_1 in the state-space model is defined as

$$A_1 = \begin{bmatrix} 0 & 0 & 1 & 0 \\ 0 & 0 & 0 & 1 \\ 0 & A_1(3,2) & A_1(3,3) & A_1(3,4) \\ 0 & A_1(4,2) & A_1(4,3) & A_1(4,4) \end{bmatrix} \tag{34}$$

The matrix B_1 in the state-space model is defined as

$$B_1 = \begin{bmatrix} 0 & 0 \\ 0 & 0 \\ B_1(3) & B_1(3) \\ B_1(4) & B_1(4) \end{bmatrix} \tag{35}$$

The matrix A_2 in the state-space model is defined as

$$A_2 = \begin{bmatrix} 0 & 1 \\ 0 & -J/I \end{bmatrix} \tag{36}$$

The matrix B_2 in the state-space model is defined as

$$B_2 = \begin{bmatrix} 0 & 0 \\ -K/I & K/I \end{bmatrix} \tag{37}$$

The variables in the A_1, A_2, B_1 and B_2 matrix are defined as

$A_1(3,2) = -gMLE(1,2)/\det(E)$, $A_1(4,2) = gMLE(1,1)/\det(E)$,

$A_1(3,3) = -2\left[(\beta + f_w)E(2,2) + \beta E(1,2)\right]/\det(E)$,

$A_1(4,3) = 2\left[(\beta + f_w)E(1,2) + \beta E(1,1)\right]/\det(E)$,

$A_1(3,4) = 2\beta[E(2,2) + E(1,2)]/\det(E)$

$A_1(4,4) = -2\beta[E(1,1) + E(1,2)]/\det(E)$

$B_1(3) = \alpha[E(2,2) + E(1,2)]/\det(E)$

$B_1(4) = -\alpha[E(1,1) + E(1,2)]/\det(E)$

$$\det(E) = E(1,1)E(2,2) - E(1,2)^2$$

The state space model of TWSBR (with parameters from table 1) is divided into two subsystems, as shown below:

The state equation of the self-balancing subsystem is as follows:

$$\begin{bmatrix} \dot{\theta} \\ \dot{\psi} \\ \ddot{\theta} \\ \ddot{\psi} \end{bmatrix} = \begin{bmatrix} 0 & 0 & 1 & 0 \\ 0 & 0 & 0 & 1 \\ 0 & 55.540 & -0.610 & 0.610 \\ 0 & 62.794 & 0.316 & -0.316 \end{bmatrix} \begin{bmatrix} \theta \\ \psi \\ \dot{\theta} \\ \dot{\psi} \end{bmatrix} + \begin{bmatrix} 0 & 0 \\ 0 & 0 \\ 9.385 & 9.385 \\ -4.857 & -4.857 \end{bmatrix} \begin{bmatrix} v_l \\ v_r \end{bmatrix} \tag{38}$$

The state equation of the steering subsystem is as follows:

$$\begin{bmatrix} \dot{\phi} \\ \ddot{\phi} \end{bmatrix} = \begin{bmatrix} 0 & 1 \\ 0 & -11.742 \end{bmatrix} \begin{bmatrix} \phi \\ \dot{\phi} \end{bmatrix} + \begin{bmatrix} 0 & 0 \\ -61.146 & 61.146 \end{bmatrix} \begin{bmatrix} v_l \\ v_r \end{bmatrix} \tag{39}$$

With the state space equations, it can be calculated that the system is completely controllable and observable.

3. Controller design

Fig.2 shows the system block diagram of the LMI-SMC method. First, TWSBR is divided into a self-balancing and steering subsystem. Then, an LMI-SMC control method is proposed to deal with the two subsystems in TWSBR. The controller of the self-balancing subsystem implements system stabilization control, while the steering subsystem implements trajectory tracking control.

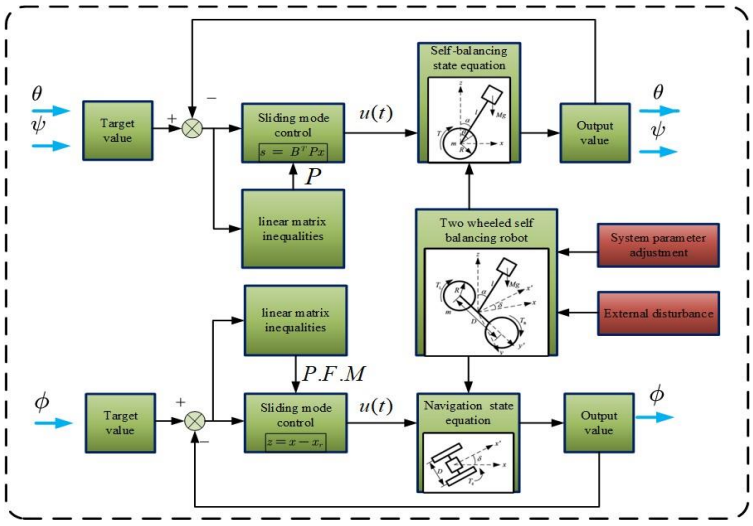

Figure 2. Block diagram of the control method of TWSBR

3.1. self-balancing system

3.1.1. System description

For the self-balancing subsystem, as in the state space equation (38), the control goal is to converge x_1 to 0, and the self-balancing system is stabilized.

3.1.2. Equivalent sliding mode control

Considering uncertainty and interference $f(x,t)$, Eq. (32) can be written as: $\dot{\mathbf{x}}_1 = \mathbf{A}_1\mathbf{x}_1 + \mathbf{B}_1(u + f(x,t))$. Where, $|f(x,t)|,, \delta_f, \varepsilon_0 > 0.$

Firstly, the sliding mode function s of sliding mode control is designed:

$$s = \mathbf{B}_1^{\mathrm{T}}\mathbf{P}\mathbf{x} \tag{40}$$

where, $\mathbf{P}$ is a 4×4 order positive definite matrix, and $s = 0$ is realized through the design of $\mathbf{P}$.

So, a sliding mode controller is designed:

$$u(t) = u_{\mathrm{eq}} + u_{\mathrm{n}} \tag{41}$$

According to the equivalent control principle, taking $f(x,t) = 0$, then from $\dot{x}(t) = \mathbf{A}_1\mathbf{x}(t) + \mathbf{B}_1 u$ and $\dot{s} = 0$, we can get $\dot{s} = \mathbf{B}_1^{\mathrm{T}}\mathbf{P}\dot{\mathbf{x}} = \mathbf{B}_1^{\mathrm{T}}\mathbf{P}(\mathbf{A}_1\mathbf{x}(t) + \mathbf{B}_1 u) = 0$.

Thereby

$$u_{\mathrm{eq}} = -(\mathbf{B}_1^{\mathrm{T}}\mathbf{P}\mathbf{B}_1)^{-1}\mathbf{B}_1^{\mathrm{T}}\mathbf{P}\mathbf{A}_1\mathbf{x}(t) \tag{42}$$

To ensure $\dot{s} < 0$, a robust control term is taken

$$u_{\mathrm{n}} = -\left(\mathbf{B}_1^{\mathrm{T}}\mathbf{P}\mathbf{B}_1\right)^{-1}\left[\left|\mathbf{B}_1^{\mathrm{T}}\mathbf{P}\mathbf{B}_1\right|\delta_{\mathrm{f}} + \varepsilon_0\right]\mathrm{sgn}(s) \tag{43}$$

Theorem 1: For the state space Eq.(38), if the sliding mode controller of the proposed Eq.(41) is used, as well as the equivalent control rate of Eq.(42) and the robust control term of Eq.(43), then the system is asymptotically stable.

Proof: Take the Lyapunov function.

$$V = \frac{1}{2}s^2 \tag{44}$$

Where,

$$\dot{s} = \mathbf{B}_1^{\mathrm{T}}\mathbf{P}\dot{\mathbf{x}}(t) = \mathbf{B}_1^{\mathrm{T}}\mathbf{P}(\mathbf{A}_1\mathbf{x}(t) + \mathbf{B}_1(u + f(x,t))) \tag{45}$$

$$= \mathbf{B}_1^{\mathrm{T}}\mathbf{P}\mathbf{A}_1\mathbf{x}(t) + \mathbf{B}_1^{\mathrm{T}}\mathbf{P}\mathbf{B}_1 u + \mathbf{B}_1^{\mathrm{T}}\mathbf{P}\mathbf{B}_1 f(x,t)$$

$$= \mathbf{B}_1^{\mathrm{T}}\mathbf{P}\mathbf{A}_1\mathbf{x}(t) + \mathbf{B}_1^{\mathrm{T}}\mathbf{P}\mathbf{B}_1\left(-\left(\mathbf{B}^{\mathrm{T}}\mathbf{P}\mathbf{B}_1\right)^{-1}\mathbf{B}_1^{\mathrm{T}}\mathbf{P}\mathbf{A}_1\mathbf{x}(t)\right.$$

$$\left.-\left(\mathbf{B}_1^{\mathrm{T}}\mathbf{P}\mathbf{B}_1\right)^{-1}\left[\left|\mathbf{B}_1^{\mathrm{T}}\mathbf{P}\mathbf{B}_1\right|\delta_{\mathrm{f}} + \varepsilon_0\right]\mathrm{sgn}(s)\right) + \mathbf{B}_1^{\mathrm{T}}\mathbf{P}\mathbf{B}_1 f(x,t)$$

$$= -\left[\left|\mathbf{B}_1^{\mathrm{T}}\mathbf{P}\mathbf{B}_1\right|\delta_{\mathrm{f}} + \varepsilon_0\right]\mathrm{sgn}(s) + \mathbf{B}_1^{\mathrm{T}}\mathbf{P}\mathbf{B}_1 f(x,t)$$

Therefore,

$$\dot{V} = s\dot{s} = -\left[\left|\mathbf{B}_1^{\mathrm{T}}\mathbf{P}\mathbf{B}_1\right|\delta_f + \varepsilon_0\right]|s| + \mathbf{B}_1^{\mathrm{T}}\mathbf{P}\mathbf{B}_1 f(x,t) \le -\varepsilon_0|s| \quad (46)$$

This completes the proof.

3.1.3. Sliding mode control based on auxiliary feedback

Use LMI to design $\mathbf{P}$.

To solve the symmetric positive definite matrix $\mathbf{P}$ in the control law, the control law formula is written as

$$u(t) = -\mathbf{K}\mathbf{x} + v(t) \quad (47)$$

where, $v(t) = \mathbf{K}\mathbf{x} + u_{\mathrm{eq}} + u_{\mathrm{n}}$

Then equation becomes

$$\dot{\mathbf{x}}(t) = \overline{\mathbf{A}_1}\mathbf{x}(t) + \mathbf{B}_1(v + f(x,t)) \quad (48)$$

where, $\overline{\mathbf{A}}_1 = \mathbf{A}_1 - \mathbf{B}_1\mathbf{K}$.

Theorem 2: $\mathbf{K}$ is designed to make $\overline{\mathbf{A}}_1$ Hurwitz, thus ensuring the stability of the closed-loop system.

Proof: Take the Lyapunov function

$$V = \mathbf{x}^{\mathrm{T}}\mathbf{P}\mathbf{x} \quad (49)$$

Therefore

$$\dot{V} = 2\mathbf{x}^{\mathrm{T}}\mathbf{P}\dot{\mathbf{x}} = 2\mathbf{x}^{\mathrm{T}}\mathbf{P}(\overline{\mathbf{A}}_1\mathbf{x}(t) + \mathbf{B}_1(v + f(x,t))) = 2\mathbf{x}^{\mathrm{T}}\mathbf{P}\overline{\mathbf{A}}_1\mathbf{x}(t) + 2\mathbf{x}^{\mathrm{T}}\mathbf{P}\mathbf{B}_1(v + f(x,t)) \quad (50)$$

From the analysis of the control law formula, it can be known that there exists $t \ge t_0, s = \mathbf{B}_1^{\mathrm{T}}\mathbf{P}\mathbf{x}(\mathbf{t}) = 0$ holds true, namely $s^{\mathrm{T}} = \mathbf{x}^{\mathrm{T}}\mathbf{P}\mathbf{B}_1 = 0$ is established, then the above formula becomes

$$\dot{V} = 2\mathbf{x}^{\mathrm{T}}\mathbf{P}\overline{\mathbf{A}}_1\mathbf{x} = \mathbf{x}^{\mathrm{T}}\left(\mathbf{P}\overline{\mathbf{A}}_1 + \overline{\mathbf{A}}_1^{\mathrm{T}}\mathbf{P}\right)\mathbf{x} \quad (51)$$

In order to ensure that $\dot{V} < 0$, we need

$$\mathbf{P}\overline{\mathbf{A}}_1 + \overline{\mathbf{A}}_1^{\mathrm{T}}\mathbf{P} < 0 \quad (52)$$

Multiply $\mathbf{P}^{-1}$ by the left and right sides of $\mathbf{P}\overline{\mathbf{A}}_1 + \overline{\mathbf{A}}_1^{\mathrm{T}}\mathbf{P}$ respectively, and get

$$\overline{\mathbf{A}}_1\mathbf{P}^{-1} + \mathbf{P}^{-1}\overline{\mathbf{A}}_1^{\mathrm{T}} < 0 \quad (53)$$

Take $\mathbf{X} = \mathbf{P}^{-1}$, then

$$\overline{\mathbf{A}}_1\mathbf{X} + \mathbf{X}\overline{\mathbf{A}}_1^{\mathrm{T}} < 0, (\mathbf{A}_1 - \mathbf{B}_1\mathbf{K})\mathbf{X} + \mathbf{X}(\mathbf{A}_1 - \mathbf{B}_1\mathbf{K})^{\mathrm{T}} < 0 \quad (54)$$

Take $\mathbf{L} = \mathbf{K}\mathbf{X}$, then

$$\mathbf{A}_1\mathbf{X}-\mathbf{B}_1\mathbf{L}+\mathbf{X}\mathbf{A}_1^{\mathrm{T}}-\mathbf{L}^{\mathrm{T}}\mathbf{B}_1^{\mathrm{T}}<0 \tag{55}$$

Then

$$\mathbf{A}_1\mathbf{X}+\mathbf{X}\mathbf{A}_1^{\mathrm{T}}<\mathbf{B}_1\mathbf{L}+\mathbf{L}^{\mathrm{T}}\mathbf{B}_1^{\mathrm{T}} \tag{56}$$

This completes the proof.

In addition, in LMI design, it is necessary to ensure that $\mathbf{P}$ is a symmetric positive definite matrix.

$$\mathbf{P}=\mathbf{P}^{\mathrm{T}}>0 \text{ or } \mathbf{X}=\mathbf{X}^{\mathrm{T}} \tag{57}$$

3.2. navigation system

3.2.1. System description

For the steering subsystem, as in the state space equation (39), the control goal is x_2 to converge to x_{r} and to achieve system trajectory tracking of the self-balancing system, where x_{r} is the ideal instruction.

3.2.2. Controller design

Define the tracking error as $z=x-x_{\mathrm{r}}$, then

$$\dot{z}=\dot{\mathbf{x}}-\dot{\mathbf{x}}_{\mathrm{r}}=\mathbf{A}_2\mathbf{x}+\mathbf{B}_2u+\mathbf{d}-\dot{\mathbf{x}}_{\mathrm{r}} \tag{58}$$

The tracking error z is designed as a sliding mode function, and the control law is designed as

$$\mathbf{u}=\mathbf{F}\mathbf{x}+\mathbf{u}_{\mathrm{r}}+\mathbf{u}_{\mathrm{s}} \tag{59}$$

Where $\mathbf{F}$ is the state feedback gain, which can be obtained by designing the LMI. Taking the feedforward control term $\mathbf{u}_{\mathrm{r}}=-\mathbf{F}\mathbf{x}_{\mathrm{r}}-\mathbf{B}_2^{-1}\mathbf{A}_2\mathbf{x}_{\mathrm{r}}+\mathbf{B}_2^{-1}\dot{\mathbf{x}}_{\mathrm{r}}$, sliding mode robust term $\mathbf{u}_{\mathrm{s}}=-\mathbf{B}_2^{-1}(\boldsymbol{\eta}\mathrm{sgn}(\mathbf{z})),\boldsymbol{\eta}\in R^{n\times 1},\eta_i>\bar{d}_i$, and $\boldsymbol{\eta}\mathrm{sgn}(\mathbf{z})=\left[\eta_1\,\mathrm{sgn}\,z_1\quad\cdots\eta_n\,\mathrm{sgn}\,z_n\right]^{\mathrm{T}}$

Then

$$\begin{aligned}\mathbf{u}&=\mathbf{F}\mathbf{x}-\mathbf{F}\mathbf{x}_{\mathrm{r}}-\mathbf{B}_2^{-1}\mathbf{A}_2\mathbf{x}_{\mathrm{r}}+\mathbf{B}_2^{-1}\dot{\mathbf{x}}_{\mathrm{r}}-\mathbf{B}_2^{-1}(\boldsymbol{\eta}\mathrm{sgn}(\mathbf{z}))\\&=\mathbf{F}\mathbf{z}-\mathbf{B}_2^{-1}\mathbf{A}_2\mathbf{x}_{\mathrm{r}}+\mathbf{B}_2^{-1}\dot{\mathbf{x}}_{\mathrm{r}}-\mathbf{B}_2^{-1}(\boldsymbol{\eta}\mathrm{sgn}(\mathbf{z}))\end{aligned} \tag{60}$$

And

$$\begin{aligned}\dot{\mathbf{z}}&=\mathbf{A}_2\mathbf{x}+\mathbf{B}_2\left(\mathbf{F}\mathbf{z}-\mathbf{B}_2^{-1}\mathbf{A}_2\mathbf{x}_{\mathrm{r}}+\mathbf{B}_2^{-1}\dot{\mathbf{x}}_{\mathrm{r}}-\mathbf{B}_2^{-1}(\boldsymbol{\eta}\mathrm{sgn}(\mathbf{z}))\right)+\mathbf{d}-\dot{\mathbf{x}}_{\mathrm{r}}\\&=\mathbf{A}_2\mathbf{x}+\mathbf{B}_2\mathbf{F}z-\mathbf{A}_2\mathbf{x}_{\mathrm{r}}+\dot{\mathbf{x}}_{\mathrm{r}}-\boldsymbol{\eta}\mathrm{sgn}(z)+\mathbf{d}-\dot{\mathbf{x}}_{\mathrm{r}}\\&=\mathbf{A}_2\mathbf{z}+\mathbf{B}_2\mathbf{F}z-\boldsymbol{\eta}\mathrm{sgn}(\mathbf{z})+\mathbf{d}\end{aligned} \tag{61}$$

Theorem 3: If the inequality is satisfied

$$\mathbf{A}_2^{\mathrm{T}}\mathbf{P}+\mathbf{M}^{\mathrm{T}}+\mathbf{P}\mathbf{A}_2+\mathbf{M}<0 \tag{62}$$

Where, $\mathbf{F}=(\mathbf{PB}_2)^{-1}\mathbf{M}$.

The closed-loop system comprising the controlled object Eq.(39) and the control law Eq.(59) is asymptotically stable.

Proof: Take the Lyapunov function

$$V=\mathbf{z}^{\mathrm{T}}\mathbf{Pz} \tag{63}$$

Where, $\mathbf{P}=\mathrm{diag}\{p_i\}$ is a diagonal matrix, $p_i>0$.

Then

$$\begin{aligned}\dot{V}&=\left(\mathbf{z}^{\mathrm{T}}\mathbf{P}\right)'\mathbf{z}+\mathbf{z}^{\mathrm{T}}\mathbf{P}\dot{\mathbf{z}}=\dot{\mathbf{z}}^{\mathrm{T}}\mathbf{Pz}+\mathbf{z}^{\mathrm{T}}\mathbf{P}\dot{\mathbf{z}}\\&=(\mathbf{A}_2\mathbf{z}+\mathbf{B}_2\mathbf{Fz}-\boldsymbol{\eta}\,\mathrm{sgn}(\mathbf{z})+\mathbf{d})^{\mathrm{T}}\mathbf{Pz}+\mathbf{z}^{\mathrm{T}}\mathbf{P}(\mathbf{A}_2\mathbf{z}+\mathbf{B}_2\mathbf{Fz}-\boldsymbol{\eta}\,\mathrm{sgn}(\mathbf{z})+\mathbf{d})\\&=\mathbf{z}^{\mathrm{T}}\mathbf{A}_2^{\mathrm{T}}\mathbf{Pz}+\mathbf{z}^{\mathrm{T}}\mathbf{F}^{\mathrm{T}}\mathbf{B}_2^{\mathrm{T}}\mathbf{Pz}+(-\boldsymbol{\eta}\,\mathrm{sgn}(\mathbf{z})+\mathbf{d})^{\mathrm{T}}\mathbf{Pz}\\&+\mathbf{z}^{\mathrm{T}}\mathbf{PA}_2\mathbf{z}+\mathbf{z}^{\mathrm{T}}\mathbf{PB}_2\mathbf{Fz}+\mathbf{z}^{\mathrm{T}}\mathbf{P}(-\boldsymbol{\eta}\,\mathrm{sgn}(\mathbf{z})+\mathbf{d})\\&\le\mathbf{z}^{\mathrm{T}}\left(\mathbf{A}_2^{\mathrm{T}}\mathbf{P}+\mathbf{F}^{\mathrm{T}}\mathbf{B}_2^{\mathrm{T}}\mathbf{P}+\mathbf{PA}_2+\mathbf{PB}_2\mathbf{F}\right)\mathbf{z}=\mathbf{z}^{\mathrm{T}}\boldsymbol{\Omega}\mathbf{z}\end{aligned} \tag{64}$$

Where,

$$\boldsymbol{\Omega}=\mathbf{A}_2^{\mathrm{T}}\mathbf{P}+\mathbf{F}^{\mathrm{T}}\mathbf{B}_2^{\mathrm{T}}\mathbf{P}+\mathbf{PA}_2+\mathbf{PB}_2\mathbf{F},(-\boldsymbol{\eta}\,\mathrm{sgn}(\mathbf{z})+\mathbf{d})^{\mathrm{T}}\mathbf{Pz}=\sum_{i=1}^{n}(-\eta_i+d_i)p_i|z_i|<0,\mathbf{z}^{\mathrm{T}}\mathbf{P}(-\boldsymbol{\eta}\,\mathrm{sgn}(\mathbf{z})+\mathbf{d})$$

$$=\sum_{i=1}^{n}(-\eta_i+d_i)p_i|z_i|<0.$$

In order to ensure $\dot{V}\le 0$, it needs to satisfy $\boldsymbol{\Omega}<0$, that is

$$\mathbf{A}_2^{\mathrm{T}}\mathbf{P}+\mathbf{F}^{\mathrm{T}}\mathbf{B}_2^{\mathrm{T}}\mathbf{P}+\mathbf{PA}_2+\mathbf{PB}_2\mathbf{F}<0 \tag{65}$$

In the LMI equation (65), since both $\mathbf{F}$ and $\mathbf{P}$ are unknown, to solve the LMI, they need to be linearized, setting $\mathbf{M}=\mathbf{PB}_2\mathbf{F}$, at this time LMI is expressed as

$$\mathbf{A}_2^{\mathrm{T}}\mathbf{P}+\mathbf{M}^{\mathrm{T}}+\mathbf{PA}_2+\mathbf{M}<0 \tag{66}$$

Through LMI, we can get $\mathbf{M}$ and $\mathbf{P}$, so we can get $\mathbf{F}=(\mathbf{PB}_2)^{-1}\mathbf{M}$.

According to $\dot{V}\le z^{\mathrm{T}}Qz\le 0$, we can know that when $\dot{V}\equiv 0$, $z\equiv 0$. According to Lasalle's invariance theorem, when t approaches infinity, z approaches zero infinitely.

This completes the proof.

4. Results and discussion

4.1. self-balancing subsystem stabilization control

The related robot self-balancing subsystem stabilization control simulation experiment was carried out in the Simulink simulation environment, which verified the effectiveness, stability, and robustness of the balanced aspect of the LMI-SMC controlled TWSBR system. The system parameters of the TWSBR during the experiment are: The sampling time is $T=10$ ms, the initial state of the system is

$\theta(0)=0,\dot{\theta}(0)=0.3,\psi(0)=0.1,\dot{\psi}(0)=0.3$, the ideal control task is $\theta(0)=0,\dot{\theta}(0)=0,$ $\psi(0)=0,\dot{\psi}(0)=0$. Use the sliding mode controller Eq.(41), and take $\delta_f=0.90,\varepsilon_0=0.10$.

In the same experimental environment, the control effects of the continuous function (th(*S*)), the sign function (sgn(*S*)), the hyperbolic tangent function (tanh(*S*)), and the saturation function (sat(*S*)) on LMI-SMC method are tested.

Based on the experimental results and image analysis presented in Fig.3, the performance of different functions in SMC can be evaluated in detail. The sign function (sgn(*S*)) exhibits severe chattering in the control input (Fig.3(e)). Although it performs well in terms of average angle and angular velocity control (Fig.3(a) and 3(b)), its practical application may lead to rapid actuator wear and the introduction of high frequency noise, thereby affecting the long-term stability and reliability of the system. The saturation function (sat(*S*)) demonstrates excellent performance across all aspects. It shows stability and minimal overshoot in average angle (Fig.3(a)), angular velocity control (Fig.3(b)), pitch angle (Fig.3(c)), and pitch angular velocity (Fig.3(d)).

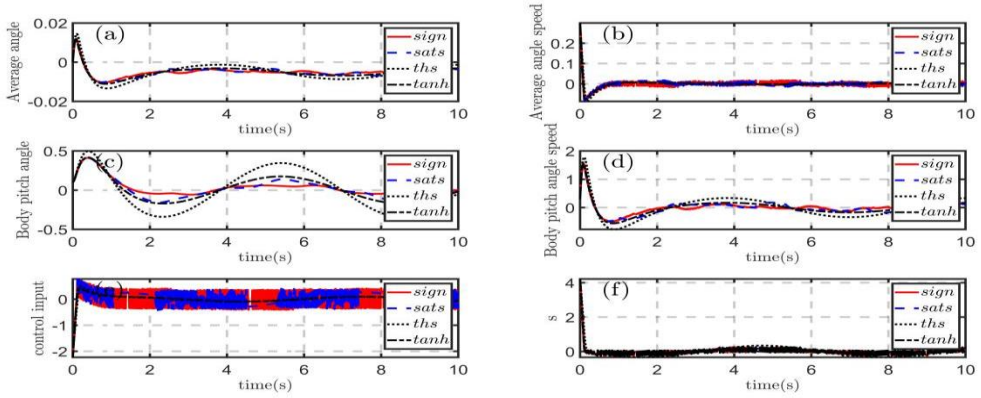

Figure 3. Control performance of different function styles. (a)The average angle of the left and right wheels. (b)Average angle speed of the left and right wheels. (c)Body pitch angle. (d)body pitch angle speed. (e)Control input. (f)Sliding surface about SMC.

Additionally, the chattering in the control input is significantly reduced (Fig.3(e)), and the sliding surface converges well (Fig.3(f)), indicating superior control performance and smoothness in SMC. The hyperbolic tangent function (tanh(*S*)) and the continuous function (th(*S*)), while exhibiting good smooth control performance, have slightly higher overshoot and slower response compared to the saturation function. In Fig.3(a)(d), tanh(*S*) and th(*S*) show lower control accuracy and dynamic response compared to the saturation function. Their control inputs are smoother, effectively suppressing chattering (Fig.3(e)), and their sliding surfaces converge well (Fig.3(f)). However, they are somewhat deficient in terms of rapid response and precision.

Therefore, considering all performance indicators, the saturation function (sat(*S*)) exhibits the best overall control performance in sliding mode control. The saturation function as the sliding mode controller in TWSBR systems is recommended to achieve superior control effects and system robustness. The saturation function is used, and the boundary layer thickness is Δ = 0.05. From Eq.(56) and Eq.(57), *X* and *L* can be solved so that we can get

$$\mathbf{P}=\begin{bmatrix}2.2161 & 0.9628 & 2.6787 & 1.7761\\ 0.9628 & 2.2159 & 1.7316 & 1.5750\\ 2.6787 & 1.7316 & 5.6874 & 3.1574\\ 1.7761 & 1.5750 & 3.1574 & 2.9177\end{bmatrix}\quad \mathbf{K}=\begin{bmatrix}12.6884 & 17.2798 & 22.4561 & 20.9620\end{bmatrix}$$

It can be verified that *K* makes A_1 Hurwitz.

4.1.1. Experiment one

To better reflect the advantages of the LMI-SMC method proposed in this article, we first compare it with the pole placement(PP), Linear Quadratic Regulator(LQR), and Robust control based on linear matrix inequalities (LMI-H_∞) methods to show the excellent control performance of the proposed method.

In Fig.4, through the analysis of experimental results, LMI-SMC shows significant performance advantages in many aspects. First, the LMI-SMC controller exhibits minimal overshoot in the control of the average wheel angle (Fig. 4(a)) and the body pitch angle (Fig. 4(c)), indicating that it has better dynamic response characteristics. The overshoot of LMI-H_∞ is the largest in the average wheel angle (Fig. 4(a)), and the overshoot of PP is the largest in the body pitch angle (Fig. 4(c)). Secondly, the overshoot of LMI-SMC in the control of the average angular velocity of the left and right wheels (Fig. 4(b)) and the body pitch angular velocity (Fig. 4(d)) is small, further demonstrating its superior performance in suppressing overshoot. In addition, the control input of the LMI-SMC controller is within the limit range of -24V to 24V (Fig. 4(e)), which meets the actual requirements of the system, while LMI-H_∞ and LQR The controller exceeded the limit, reaching 31v and -43v respectively, which is not ideal. Finally, the good convergence of LMI-SMC on the sliding surface (Fig. 4(f)) shows that it has strong robustness and control accuracy. In summary, the LMI-SMC method shows excellent performance in various control scenarios, verifying its feasibility and superiority as an efficient control method for two-wheeled self-balancing robot systems.Tab. 2 shows the parameter selection of different controller types and optimized controllers' gains.

Table 2. Parameter selection of the LMI-SMC,PP,*LQR* and *LMI* $-H_\infty$ controller and determination of the K value.

Controller Type	Parameters	K
PP	ζ=0.5, ω_n=3, p=[-1.5-2.6i, -1.5+2.6i, -8, -10]	K=[0.8391, 8.2436, 0.4079, 0.2342]
LQR	$\mathbf{Q}=\begin{bmatrix}10000 & 0 & 0 & 0\\ 0 & 1 & 0 & 0\\ 0 & 0 & 10000 & 0\\ 0 & 0 & 0 & 1\end{bmatrix}$, R=1	K=[100.0000, 20.8668, 105.6967, 5.9927]
LMI-SMC	δf=0.90, ε_0=0.10	K=[12.6884, 17.2798, 22.4561, 20.9620]
LMI $-H_\infty$	q_1=1.0, q_2=1.0, q_3=1.0, q_4=1.0, ρ=1	K=[1.7546, 95.8777, 1.7977, 10.6114]

4.1.2. Experiment two

During the self-balancing control process of TWSBR, external impacts and other interferences make it easy to be disturbed, causing the load to shake unexpectedly. The purpose of this experiment is to verify the robustness of LMI-SMC. This paper designs and simulates external interference. During the simulation process, artificial interference $f(t) = 0.3\sin t$ is added to affect the control performance of the controller.

This experiment aims to verify the robustness of the LMI-SMC method under external disturbance conditions. The performance of the controller is affected by adding artificial disturbance $f(t) = 0.3\sin t$ during the simulation process. Fig. 5 shows the control performance of different optimized controllers under disturbance conditions. The results show that the LMI-SMC controller performs well in many indicators. Specifically, LMI-SMC maintains minimal fluctuations and overshoots in the control of the average angle and the average angular velocity of the left and right wheels, showing high control accuracy and stability (Fig. 5(a) and Fig. 5(b)). In contrast, the LMI-H_∞ and PP controllers exhibited large fluctuations and overshoots after the addition of disturbances, and the

control accuracy decreased significantly (Fig. 5(a) and Fig. 5(c)). In addition, the control input of the LMI-SMC controller is within the limit range of -24V to 24V, which meets the actual requirements of the system, while the LMI-H_∞ and LQR controllers exceed this limit in the early stage of control, affecting the reliability and safety of the system (Fig. 5(e)). Finally, the good convergence of LMI-SMC on the sliding surface (Fig. 5(f)) further proves its robustness and control accuracy. In summary, the LMI-SMC method shows excellent control performance under external disturbance conditions, verifying its feasibility and superiority as an efficient control method for the two-wheeled self-balancing robot system.

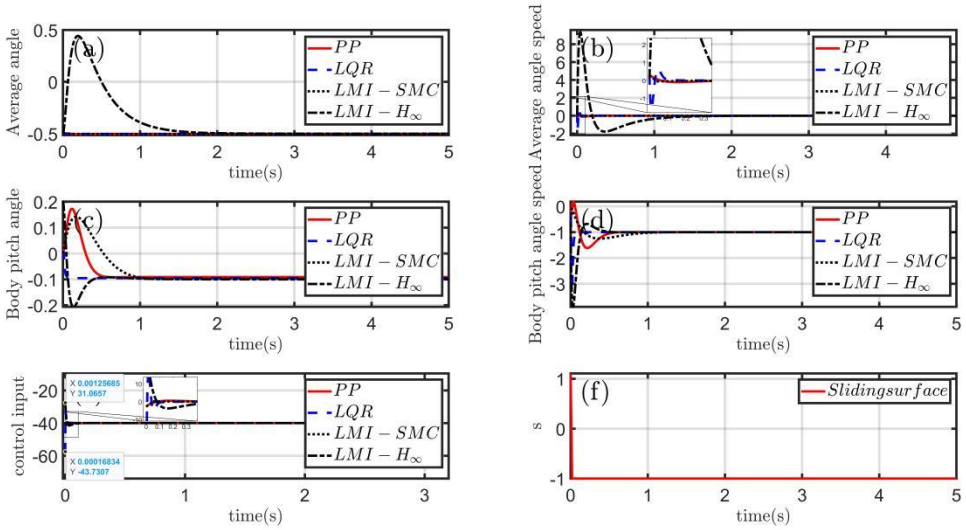

Figure 4. Control performance of different types of controllers. (a)The average angle of the left and right wheels. (b)Average angle speed of the left and right wheels. (c)Body pitch angle. (d)body pitch angle speed. (e)Control input. (f)Sliding surface about SMC.

4.1.3. Experiment three

The payload mass and robot height are changed to verify the robustness of the proposed control method to parameter uncertainty.

(1) The payload mass M suddenly changes from 0.2kg to 0.3kg, while the wheel mass m remains at 0.065kg.

(2) The TWSBR height suddenly changes from 0.14m to 0.20m.

This paper analyzes in detail the control performance of four control methods (LMI-H_∞, LQR, PP and LMI-SMC) under three conditions: constant parameters (N-turning), weight adjustment (M-turning) and height adjustment (H-turning), and further verifies the robustness under different parameter changes. The specific experimental conditions are that the payload mass M changes from 0.2kg to 0.3kg, or the TWSBR height changes from 0.14m to 0.20m. In both cases, when the above four control methods are used as controllers, the control gain parameters remain unchanged. The experimental results of Fig.6, Fig.7, Fig.8, and Fig.9 show that the LMI-SMC control method (Fig.8) exhibits good control performance under all parameter adjustments. It performs best in terms of stability and control accuracy of the average angle of the left and right wheels, the average angular velocity, the pitch angle of the vehicle body, and the pitch angular velocity of the vehicle body, and the fluctuation of the control input is also the smallest. In contrast, the LMI-H_∞ (Fig.9) and PP control methods (Fig.6) fluctuate greatly after parameter adjustment, and overshoot occurs, especially when adjusting the height, the system stability and control accuracy are significantly reduced. The LQR control method (Fig.7) maintains the stability of the system to a certain extent, but the control input still fluctuates.

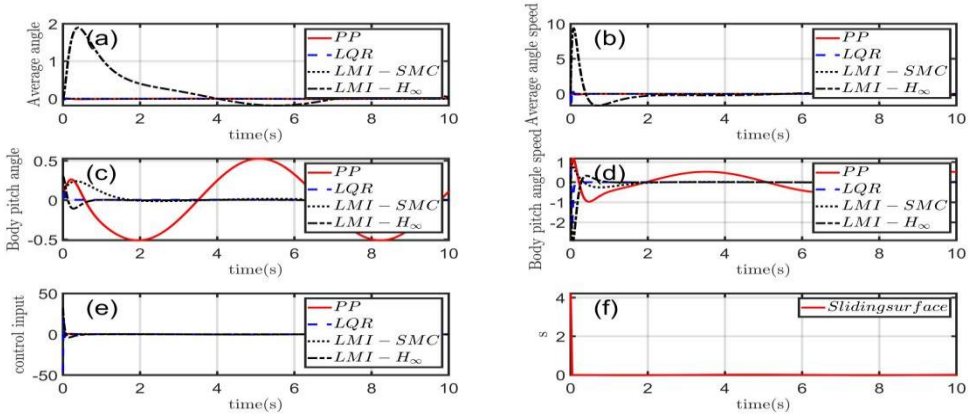

Figure 5. Control performance of different types of controllers with interference $f(t) = 0.3\sin t$. (a)The average angle of the left and right wheels. (b)Average angle speed of the left and right wheels. (c)Body pitch angle. (d)body pitch angle speed. (e)Control input. (f)Sliding surface about SMC.

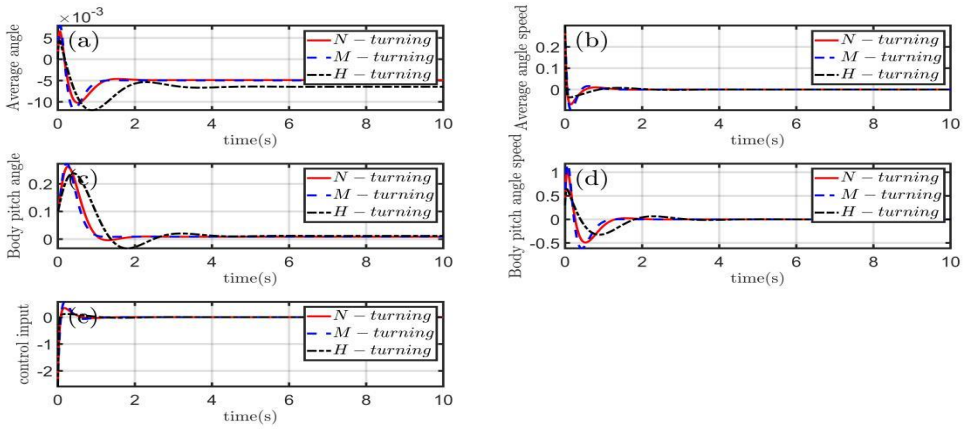

Figure 6. Performance of PP controller after robot parameters change. (a)The average angle of the left and right wheels. (b)Average angle speed of the left and right wheels. (c)Body pitch angle. (d)Body pitch angle speed. (e)Control input.

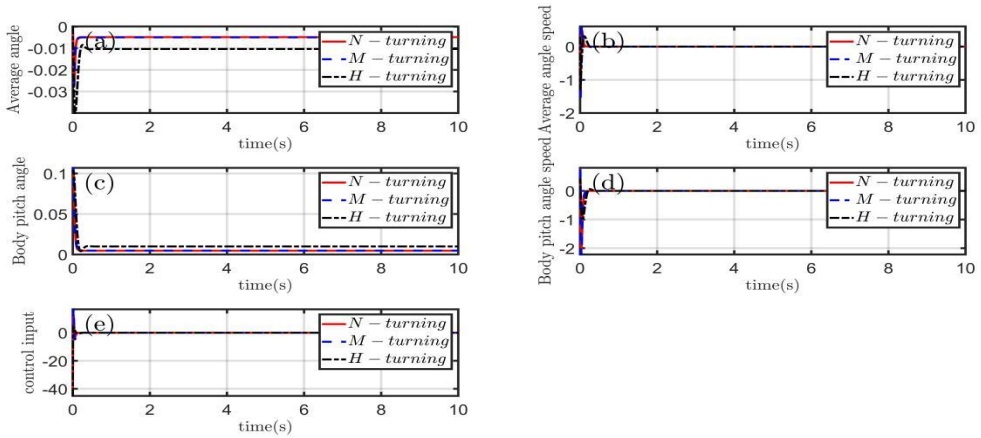

Figure 7. Performance of LQR controller after robot parameters change. (a)The average angle of the left and right wheels. (b)Average angle speed of the left and right wheels. (c)Body pitch angle. (d)Body pitch angle speed. (e)Control input.

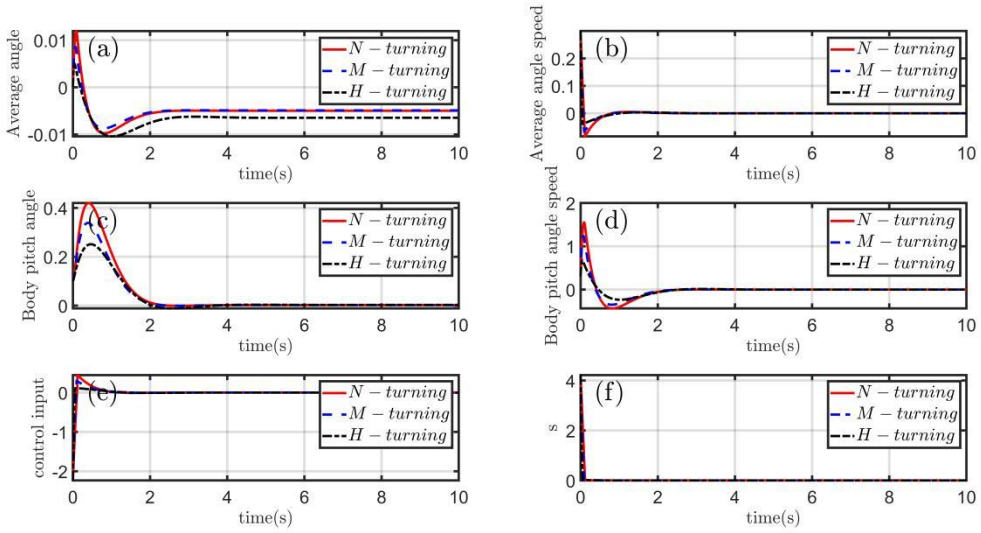

Figure 8. Performance of LMI-SMC controller after robot parameters change. (a)The average angle of the left and right wheels. (b) Average angle speed of the left and right wheels. (c)Body pitch angle. (d)Body pitch angle speed. (e)Control input. (f)Sliding surface about SMC.

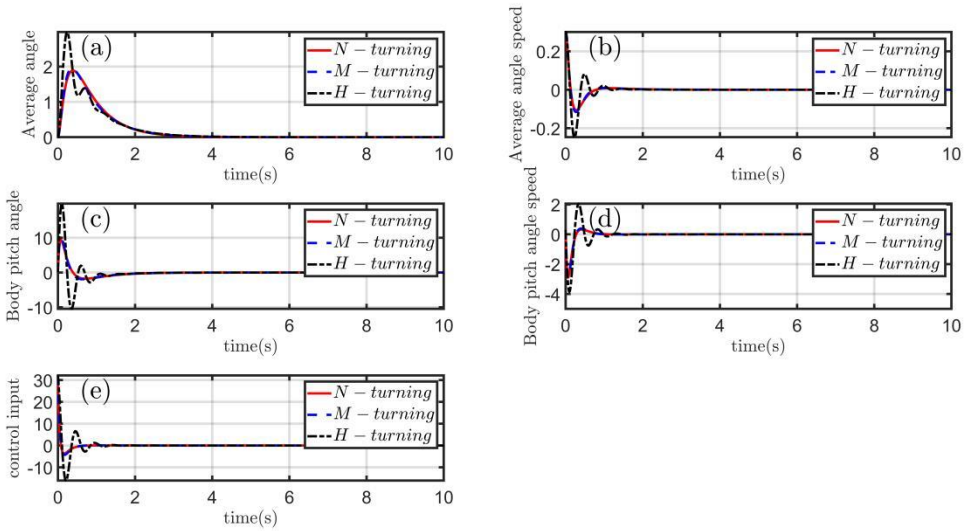

Figure 9. Performance of LMI-H_∞ controller after robot parameters change. (a)The average angle speed of the left and right wheels. (b)The average angle of the left and right wheels. (c)Body pitch angle. (d)Body pitch angle speed. (e)Control input.

The robustness verification of load mass and height changes further demonstrates the superiority of the LMI-SMC method in handling parameter uncertainty, ensuring the stability and control accuracy of the system under various parameter changes, thereby verifying its feasibility and superiority as an efficient two-wheeled self-balancing robot system control method.

4.2. Steering subsystem trajectory tracking

A related robot steering subsystem trajectory tracking simulation experiment was conducted in the Simulink simulation environment, which verified the effectiveness, stability, and robustness of the steering trajectory tracking in the LMI-SMC control TWSBR system. We can get the values of the state equations A_2 and B_2 for the

controlled object Eq.(39). The ideal instructions for the two states are $[\sin t \quad \cos t]$, and the corresponding interferences are $[50\sin t \quad 50\sin t]^{\mathrm{T}}$.

To solve the LMI Eq.(66), take

$$\mathbf{P}=\begin{bmatrix}100000 & 0\\ 0 & 100000\end{bmatrix}$$

we can get

$$\mathbf{F}=\begin{bmatrix}0.0041 & 32.9711\\ -0.0041 & -32.9711\end{bmatrix}$$

using the control Eq.(60), take $\boldsymbol{\eta}=[50 \quad 50]^{\mathrm{T}}$,

When tracking the steering subsystem's trajectory, the self-balancing subsystem's saturation function is also used, and the boundary layer is $\Delta = 0.05$. In order to better reflect the advantages of the LMI-SMC method proposed in this paper, we compare it with pole placement (PP), linear quadratic regulator (LQR) and robust control based on linear matrix inequality (LMI-H_∞) methods to demonstrate the excellent control performance of the proposed method.

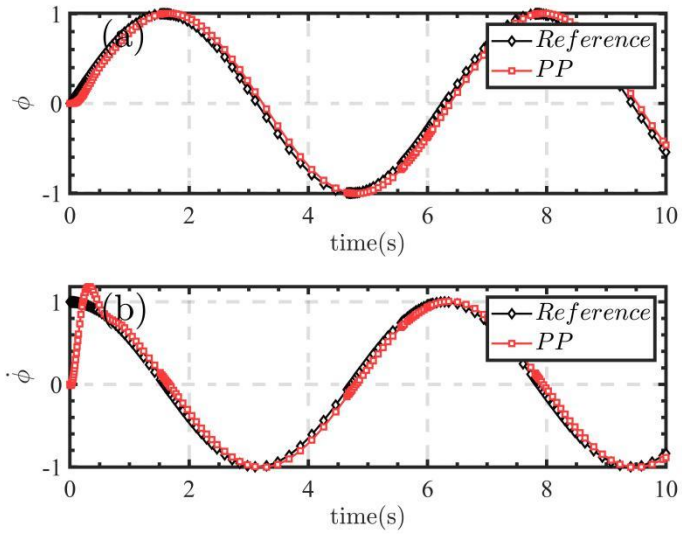

Figure 10. Trajectory tracking performance of PP

Fig.10(a) and Fig.10(b) show the trajectory tracking performance of the PP method. Although it has good trajectory tracking ability, it has a large overshoot phenomenon and a slow initial response speed; Fig.11(a) and Fig.11(b) show the trajectory tracking performance of the LQR method, which shows good trajectory tracking control performance, fast response speed and small overshoot; Fig.12(a) and Fig.12(b) show the trajectory tracking performance of the LMI-SMC method, which performs best, has fast response speed and high-precision trajectory tracking ability, and almost no overshoot. Fig.13(a) and Fig.13(b) show the trajectory tracking performance of the LMI-H_∞ method. This method has low control accuracy and poor trajectory tracking performance. Comprehensive comparison shows that the LMI-SMC method performs best in trajectory tracking control, verifying its feasibility and superiority as an efficient control method.

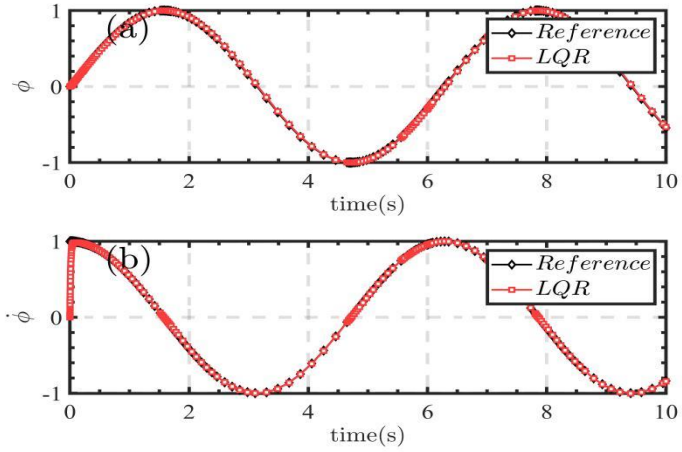

Figure 11. Trajectory tracking performance of LQR

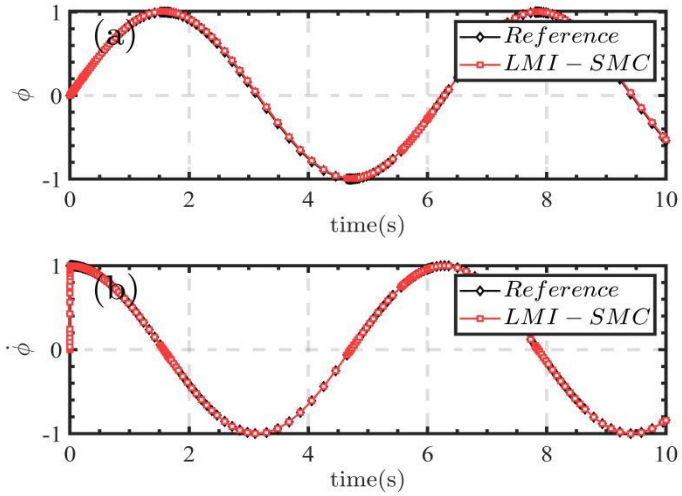

Figure 12. Trajectory tracking performance of LMI-SMC

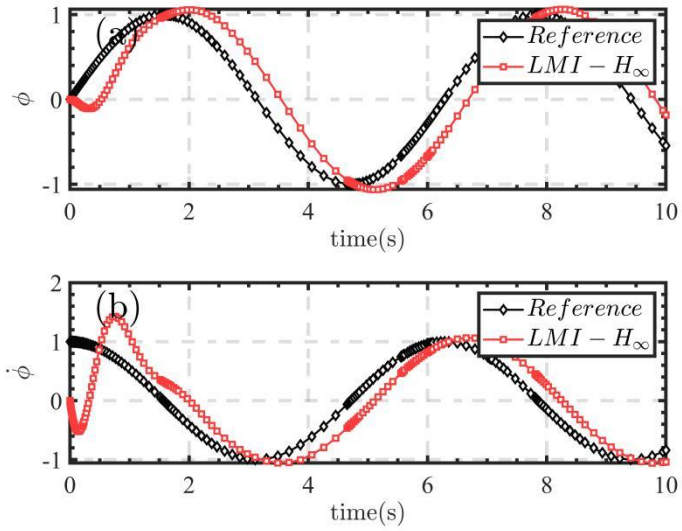

Figure 13. Trajectory tracking performance of $LMI - H_\infty$

4.3. Evaluation system

Since the controller control indicators are highly related to the robot dynamics, the evaluation indicators proposed include the average angle error of the left and right wheels of the self-balancing system as $e_{\text{wheel}} = \theta$, and the pitch angle tracking error as $e_{pitch} = \psi$. Similarly, the steering angle tracking error of the steering subsystem is $e_{yaw} = \phi$, where θ and ψ are the I_{th} coordinates of the left and right wheel average angle and body pitch angle in the world coordinate system, respectively. ϕ is the I_{th} coordinate of the robot's steering angle in the world coordinate system.

1) The integrated absolute pitch error and wheel angle rate error (IATE) are:

$$\text{IATE} = \int_0^t \left(\left| e_{\text{wheel}} \right| + \left| e_{\text{pitch}} \right| \right) dt. \tag{67}$$

2) The integration time product of absolute pitch angle error and wheel angle rate error (IAPE) is:

$$\text{IAPE} = \int_0^t t \left(\left| e_{\text{wheel}} \right| + \left| e_{\text{pitch}} \right| \right) dt. \tag{68}$$

3) The integral of the absolute value of the yaw angle (IASA) is:

$$\text{IASA} = \int_0^t \left| e_{\text{yaw}} \right| dt. \tag{69}$$

Where t is the control duration. IAPE is in addition to IATE, which does not consider duration. To make the above indicators more universal and objective, the dimensionless comprehensive weighted performance evaluation index (CWPEI) is defined as

$$\text{CWPEI} = \frac{\omega_1}{\max\left(\left| e_{\text{wheel}} \right|, \left| e_{\text{pitch}} \right| \right) t} \text{IATE} + \frac{\omega_2}{\max\left(\left| e_{\text{wheel}} \right|, \left| e_{\text{pitch}} \right| \right) t^2} \text{IAPE} + \frac{\omega_3}{\left| e_{\text{yaw}} \right|_{\max} t} \text{IASA} \tag{70}$$

Where ω_1, ω_2 and ω_3 are the weights of three user-defined indicators, respectively, $\omega_1 + \omega_2 + \omega_3 = 1$. The value of $\max\left(\left| e_{\text{wheel}} \right|, \left| e_{\text{pitch}} \right| \right)$ can be set according to the experimental results. $\left| e_{\text{yaw}} \right|_{\max}$ represents the maximum steering angle. Since the quantitative performance of the three indicators is not equally important in the evaluation, the weights ω_1, ω_2 and ω_3 were set to values such as 0.3, 0.5, and 0.2, respectively, in this simulation test. The weights are chosen to penalize lateral tracking errors and minimize control inputs. The controller's performance improves as the CWPEI value decreases.

Table 3. CWPEI fluctuations under different controllers

Exp.	Controller	IATE	IAPE	IASA	CWPEI
1	PP	0.267	0.733	0.62	19.21%
	LQR	0.104	0.488	0.089	18.19%
	LMI-SMC	0.301	0.5	0.105	18.82%
	LMI-H∞	5.809	4.373	2.385	23.61%

2	PP-INTER	3.204	15.953	0.62	43.32%
	LQR-INTER	0.102	0.483	0.089	18.13%
	LMI-SMC-INTER	0.343	0.79	0.105	19.97%
	LMI-H∞-INTER	7.648	15.656	2.385	54.80%
3	PP-H	0.379	1.024	0.62	21.83%
	PP-W	0.274	0.726	0.62	19.43%
	LQR-H	0.213	1.016	0.089	24.03%
	LQR-W	0.102	0.479	0.089	19.12%
	LMI-SMC-H	0.375	0.679	0.105	19.88%
	LMI-SMC-W	0.397	0.566	0.105	19.41%
	LMI-H∞-H	8.417	4.834	2.385	32.91%
	LMI-H∞-W	5.926	4.402	2.385	26.51%

To check the robustness of the controller, the controller performance evaluation index CWPEI is calculated, as shown in Fig.(14). The fluctuation of CWPEI can be calculated using the percentage change of CWPEI:

$$Per_{\text{Controller}} = \frac{|\max(\text{CWPEI}) - \min(\text{CWPEI})|}{\max(\text{CWPEI})} \tag{71}$$

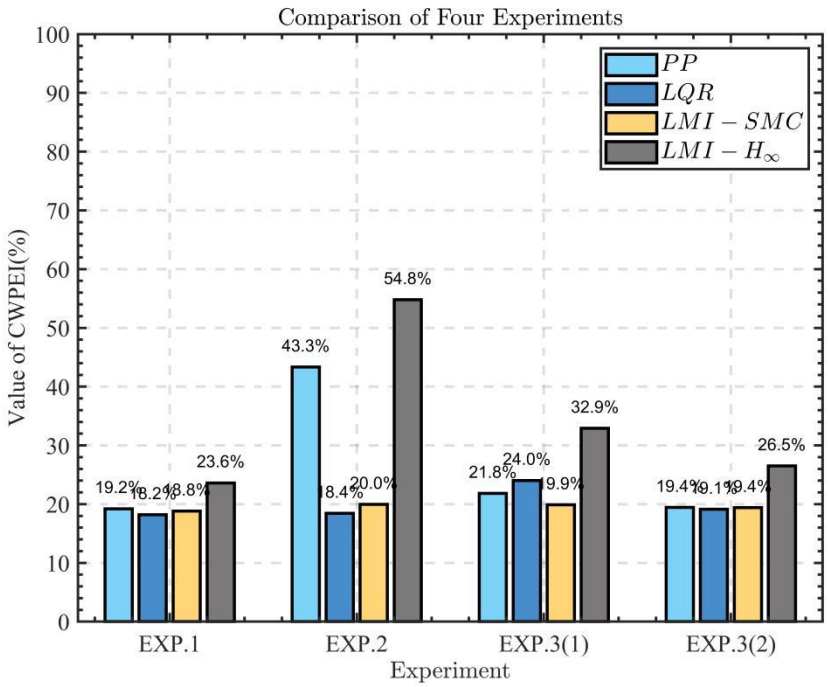

Figure 14. CWPEI in robustness test for different controllers.

Fig.14 shows that $Per_{\text{LMI-SMC}}$ (5.76%)is smaller than Per_{PP}, Per_{LQR} , and $Per_{\text{LMI-H}_\infty}$ increased by 55.66%, 24.30% and 56.92% respectively. Based on the simulation results and overall performance analysis, the proposed LMI-SMC outperforms the PP controller, LQR, and LMI-H_∞.

5. simscape Results analysis

To prove the superiority of our proposed LMI-SMC controller, we conducted a simulated 3D simulation model of TWSBR to verify our proposed controller's feasibility more intuitively. Fig.15 shows the 3D model established through simscape and Fig.16 shows the procedure for establishing the 3D model.

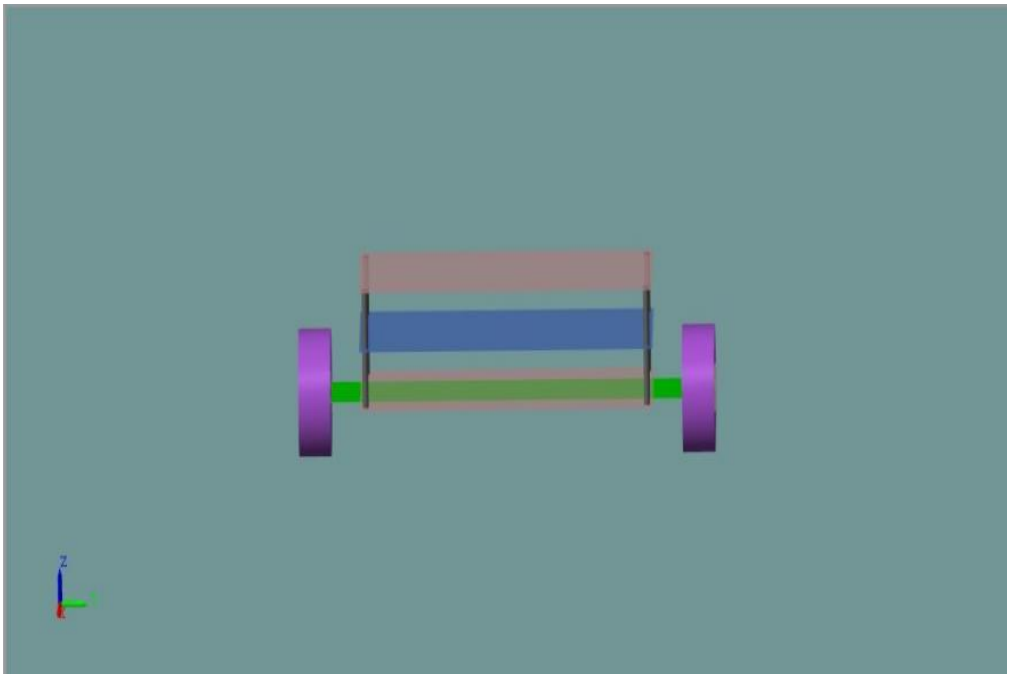

Figure 15. 3D-model of TWSBR

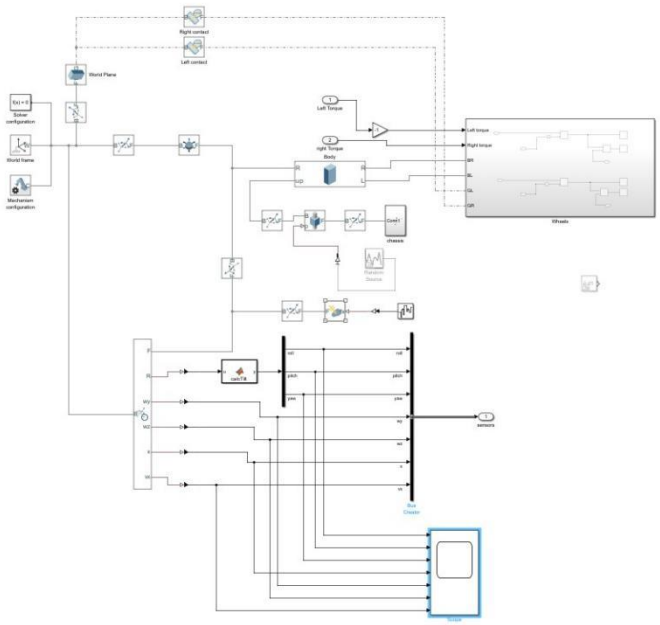

Figure 16. Simulation block of the 3D-model

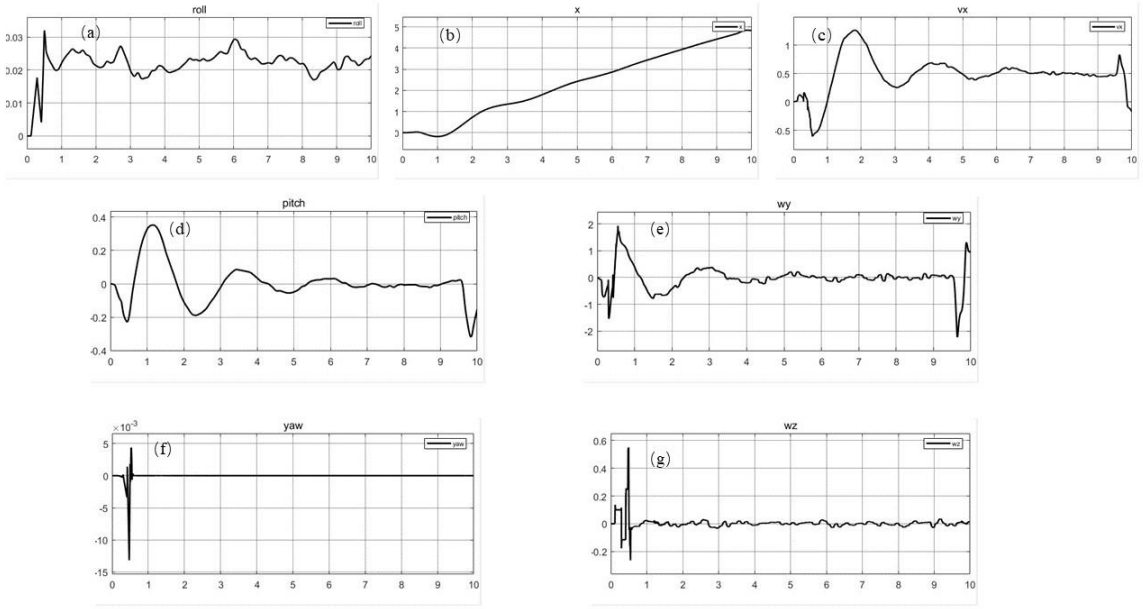

Figure 17. Performance of 3D model application controller LMI-SMC for TWSBR

In order to more accurately simulate the experimental environment, we adjusted the dynamic friction coefficient between the left and right wheels and the ground to 0.3, the static friction coefficient to 0.5, added noise interference, and used the LMI-SMC controller to make the three-dimensional model of the TWSBR travel 5 meters.

The experimental results are shown in Fig.17. Fig.17(a) shows that the roll angle fluctuates within a small range of about 0.03 during driving, indicating that the LMISMC controller can effectively suppress the fluctuation of the roll angle and ensure the lateral stability of the system; Fig.17(b) shows that the TWSBR travels about 4.8 meters smoothly in 10 seconds, close to the set 5-meter target, proving that the LMI-SMC controller can achieve relatively accurate displacement control under friction and noise interference; Fig.17(c) shows the speed curve. The speed of the TWSBR rises rapidly to about 0.5 m/s in the initial stage and remains relatively stable near this speed, verifying the effectiveness of the LMI-SMC controller in speed control; Fig.17(d) shows that the pitch angle rises rapidly to about 0.4 at startup, and then gradually decreases and tends to stabilize, indicating that the TWSBR has a slight tilt during startup, but under the action of the LMI-SMC controller, it can quickly recover and maintain an upright state; Fig.17(e) shows that the pitch angular velocity gradually stabilizes after a peak at startup, indicating that the LMI-SMC controller can effectively control the fluctuation of the pitch angular velocity and ensure the pitch stability of the system; Fig.17(f) shows that the yaw angle is basically kept near zero during the entire driving process, Fig.17(g) shows that the yaw angular velocity has a small fluctuation in the initial stage and then quickly tends to zero, indicating that the LMI-SMC controller can effectively suppress the change of the yaw angle and its velocity, ensuring that the system travels along the predetermined trajectory. In summary, the LMI-SMC controller can maintain the stability and control accuracy of the TWSBR in a complex environment containing dynamic friction, static friction and noise interference, verifying its feasibility and superiority in practical applications.

4. Conclusion

This paper designs a new sliding mode control method based on linear matrix inequality optimization. First, the motor mathematical model is combined with the Lagrangian equation of motion to re-establish the dynamic model of TWSBR. Then, based on the dynamic model, a new sliding mode control method based on linear matrix inequality optimization is designed, and the stability of TWSBR system is proved by using the Lyapunov theorem. Finally, the simulation experiment of the sliding mode control method and the stability

experiment of TWSBR are carried out, and a detailed comparison is made with other typical control methods. The simulation and experimental results show that the linear matrix inequality sliding mode controller can reduce the steady-state error, improve the control accuracy, and have good robustness.

In future research, considering the chattering nature of the sliding mode control, this method can be used as a nominal system and fuzzified through fuzzy control, thereby reducing the system chattering and the uncertainty of the system parameters.

Declaration of Conflicting Interests

The author(s) declared no potential conflicts of interest with respect to the research, author-ship, and/or publication of this article.

Data Sharing Agreement

The datasets used and/or analyzed during the current study are available from the corresponding author on reasonable request.

Funding

The author(s) received no financial support for the research, authorship, and/or publication of this article.

References

[1] F. Rubio, F. Valero, and C. Llopis-Albert, "A review of mobile robots: Concepts, methods, theoretical framework, and applications," *International Journal of Advanced Robotic Systems*, vol. 16, no. 2, p. 1729881419839596, 2019.

[2] S. Zhang, J.-t. Yao, Y.-b. Wang, Z.-s. Liu, Y.-d. Xu, and Y.-s. Zhao, "Design and motion analysis of reconfigurable wheel-legged mobile robot," *Defence Technology*, vol. 18, no. 6, pp. 1023–1040, 2022.

[3] Y. Guo, J. Guo, L. Liu, Y. Liu, and J. Leng, "Bioinspired multimodal soft robot driven by a single dielectric elastomer actuator and two flexible electroadhesive feet," *Extreme Mechanics Letters*, vol. 53, p. 101720, 2022.

[4] M. B. Khan, T. Chuthong, C. D. Do, M. Thor, P. Billeschou, J. C. Larsen, and P. Manoonpong, "icrawl: an inchworm-inspired crawling robot," *IEEE Access*, vol. 8, pp. 200655– 200668, 2020.

[5] P. Wang, Q. Tang, T. Sun, and R. Dong, "Research on stability of the four-wheeled robot for emergency obstacle avoidance on the slope," *Recent patents on engineering*, no. 5, p. 15, 2021.

[6] Y. Olmez, G. O. Koca, and Z. H. Akpolat, "Clonal selection algorithm based control for two-wheeled self-balancing mobile robot," *Simulation modelling practice and theory: International journal of the Federation of European Simulation Societies*, no. 118-, p. 118, 2022.

[7] F. Nker, "Proportional controlled moment of gyroscope for two-wheeled self-balancing robot," *Journal of Vibration and Control*, 2021.

[8] E. H. Karam, R. Habeeb, and N. M. Mjeed, "A new approach in design of sliding mode controller by optimization state feedback for two wheeled self balancing robot," *Laboratory of Open Information Technologies of the Faculty of Computational Mathematics and Mathematics of Moscow State University. M.V. Lomonosov*, no. 10, 2020.

[9] V. Mudeng, B. Hassanah, Y. T. K. Priyanto, and O. Saputra, "Design and simulation of two-wheeled balancing mobile robot with pid controller," 2020.

[10] J. Velagi´c, I. Kova˘c, A. Panjevi´c, and A. Osmanovi´c, "Design and control of two-wheeled and self-balancing mobile robot," in *2021 International Symposium ELMAR*. IEEE, 2021, pp. 77–82.

[11] C. Iwendi, M. A. Alqarni, J. H. Anajemba, A. S. Alfakeeh, and A. K. Bashir, "Robust navigational control of a two-wheeled self-balancing robot in a sensed environment," *IEEE Access*, vol. PP, no. 99, pp. 1–1, 2019.

[12] H. A. Jeyed and A. Ghaffari, "A nonlinear optimal control based on the sdre technique for the two-wheeled self-balancing robot," *Australian Journal of Mechanical Engineering*, 2020.

[13] D. Y. Gao, P. W. Han, D. S. Zhang, and Y. J. Lu, "Study of sliding mode control in self-balancing two-wheeled inverted car," *Applied Mechanics and Materials*, vol. 241, pp. 2000–2003, 2013.

[14] A. Ghahremani and A. K. Khalaji, "Simultaneous regulation and velocity tracking control of a two-wheeled self-balancing robot," in *2023 International Conference on Control, Automation and Diagnosis (ICCAD)*. IEEE, 2023, pp. 1–6.

[15] I. Jmel, H. Dimassi, S. Hadj-Said, and F. M'Sahli, "Sliding mode control for two wheeled inverted pendulum under terrain inclination and disturbances," in *2021 9th International Conference on Systems and Control (ICSC)*. IEEE, 2021, pp. 467–471.

[16] M. S. Arani, H. E. Orimi, W.-F. Xie, and H. Hong, "Comparison of sliding mode controller and state feedback controller having linear quadratic regulator (lqr) on a two-wheel inverted pendulum robot: Design and experiments," 2018.

[17] A. Sinha, P. Prasoon, P. K. Bharadwaj, and A. C. Ranasinghe, "Nonlinear autonomous control of a two-wheeled inverted pendulum mobile robot based on sliding mode," in *2015 International Conference on Computational Intelligence and Networks*. IEEE, 2015, pp. 52–57.

[18] F.-C. Paulescu, I. Szeidert, I. Filip, and C. Vasar, "Two-wheeled self-balancing robot," in *2021 IEEE 15th International Symposium on Applied Computational Intelligence and Informatics (SACI)*. IEEE, 2021, pp. 000033–000038.

[19] T. Nikita and K. Prajwal, "Pid controller based two wheeled self balancing robot," in *2021 5th International Conference on Trends in Electronics and Informatics (ICOEI)*. IEEE, 2021, pp. 1–4.

[20] B. Karthika and V. Jisha, "Nonlinear optimal control of a two wheeled self balancing robot," in *2020 5th IEEE International Conference on Recent Advances and Innovations in Engineering (ICRAIE)*. IEEE, 2020, pp. 1–6.

[21] L. M. M. Thwin and Y. Chan, "Application of lqr control for two-wheel self-balancing robot," *Myanmar Acad. Arts Sc*, 2020.

[22] J. Borja, I. Alvarado, and D. M. de la Pen˜a, "Low cost two-wheels self-balancing robot for control education powered by stepper motors," *IFAC-PapersOnLine*, vol. 53, no. 2, pp. 17518–17523, 2020.

[23] R. Liyanage, B. Annasiwattha, V. De Silva, and G. Jayamaha, "Two wheeled selfbalancing robot simulator for distance learning experiments," in *2021 10th International Conference on Information and Automation for Sustainability (ICIAfS)*. IEEE, 2021, pp. 99–104.

[24] K. Fathoni, A. P. Pratama, N. A. Salim, and V. N. Sulistyawan, "Implementasi kendali keseimbangan gerak two wheels self balancing robot menggunakan fuzzy logic," *Jurnal Teknik Elektro*, vol. 13, no. 2, pp. 89–97, 2021.

[25] O. S. Bhatti, M. Rizwan, P. S. Shiokolas, and B. Ali, "Genetically optimized anfis-based pid controller design for posture-stabilization of self-balancing-robots under depleting battery conditions," *Journal of Control Engineering and Applied Informatics*, vol. 21, no. 4, pp. 22–33, 2019.

[26] B. Shi, S. Xu, and G. Zhao, "Variable universe type-ii fuzzy logic control design for the googol's two-wheeled self-balancing robot," in *2020 Chinese automation congress (CAC)*. IEEE, 2020, pp. 1500–1505.

[27] T. Zhao, Q. Yu, S. Dian, R. Guo, and S. Li, "Non-singleton general type-2 fuzzy control for a two-wheeled self-balancing robot," *International Journal of Fuzzy Systems*, vol. 21, pp. 1724–1737, 2019.

[28] D.-M. Nguyen, N. Van-Tiem, and T.-T. Nguyen, "A neural network combined with sliding mode controller for the two-wheel self-balancing robot," *IAES International Journal of Artificial Intelligence*, vol. 10, no. 3, p. 592, 2021.

[29] A. Chhotray and D. R. Parhi, "Navigational control analysis of two-wheeled self-balancing robot in an unknown terrain using back-propagation neural network integrated modified dayani approach," *Robotica*, vol. 37, no. 8, pp. 1346–1362, 2019.

[30] V. B. V. Nghia, T. Van Thien, N. N. Son, and M. T. Long, "Adaptive neural sliding mode control for two wheel self balancing robot," *International journal of dynamics and control*, vol. 10, no. 3, pp. 771–784, 2022.

[31] A. Maity and S. Bhargava, "Design and implementation of a self-balancing two-wheeled robot driven by a feed-forward backpropagation neural network," *Int. Res. J. Eng. Technol*, vol. 7, pp. 3876–3881, 2020.

[32] S. Irfan, A. Mehmood, M. T. Razzaq, and J. Iqbal, "Advanced sliding mode control techniques for inverted pendulum: Modelling and simulation," *Engineering science and technology, an international journal*, vol. 21, no. 4, pp. 753–759, 2018.

[33] N. Zheng, Y. Zhang, Y. Guo, and X. Zhang, "Hierarchical fast terminal sliding mode control for a self-balancing two-wheeled robot on uneven terrains," in *2017 36th Chinese Control Conference (CCC)*. IEEE, 2017, pp. 4762–4767.

[34] J. F. S. Trentin and D. A. Santos, "Predefined-time global sliding mode control design for a 3d pendulum," *Nonlinear Dynamics*, vol. 109, no. 3, pp. 1693–1704, 2022.

[35] J.-X. Chen, N. He, and L. He, "Adaptive double fuzzy anti-integral saturation pid control for self-balancing robot with reaction wheel," in *2022 IEEE 17th International Conference on Control & Automation (ICCA)*. IEEE, 2022, pp. 56–61.

[36] B. CHO and R. BANG, "A pd sliding mode controller for two-wheeled self-balancing robot."

[37] J. Tian, J. Ding, Y. Tai, and Z. Ma, "Control of different-axis two-wheeled self-balancing vehicles," *IEEE Access*, vol. 8, pp. 158839–158851, 2020.

[38] Z. B. Hazem, M. J. Fotuhi, and Z. Bingu¨l, "Development of a fuzzy-lqr and fuzzy-lqg stability control for a double link rotary inverted pendulum," *Journal of the Franklin Institute*, vol. 357, no. 15, pp. 10529–10556, 2020.

[39] S. Khatoon, D. K. Chaturvedi, N. Hasan, and M. Istiyaque, "Optimal controller design for two wheel mobile robot," in *2018 3rd International Innovative Applications of Computational Intelligence on Power, Energy and Controls with their Impact on Humanity (CIPECH)*. IEEE, 2018, pp. 1–5.

[40] A. Aldhalemi, A. Chlaihawi, and A. Al-Ghanimi, "Design and implementation of a remotely controlled two-wheel self-balancing robot," in *IOP conference series: Materials science and engineering*, vol. 1067, no. 1. IOP Publishing, 2021, p. 012132.

[41] D. Singh and P. Padhy, "Design and tuning of pi λ d μ controller for higher order process using pso-nm," in *2017 Innovations in Power and Advanced Computing Technologies (iPACT)*. IEEE, 2017, pp. 1–5.

[42] G. S. Krishna, D. Sumith, and G. Akshay, "Epersist: A two-wheeled self balancing robot using pid controller and deep reinforcement learning," in *2022 22nd International Conference on Control, Automation and Systems (ICCAS)*. IEEE, 2022, pp. 1488–1492.

[43] N. M. Tahir, M. Muhammad, M. Idi, S. Buyamin, L. Maijama'a *et al.*, "Comparative analysis of observer-based lqr and lmi controllers of an inverted pendulum," *Bulletin of Electrical Engineering and Informatics*, vol. 9, no. 6, pp. 2244–2252, 2020.

[44] M. Sasaki, H. Tochigi, W. Njeri, H. Hayashi, J. Muguro, K. Matsushita, and H. Ngetha, "Robust posture tracking control of stable coaxial two-wheeled agv using the approximate inverse system and lmi," *J. Appl. Sci. Eng. Technol. Dev*, pp. 24–42, 2020.

[45] T. He, X. Chen, and G. G. Zhu, "A dual-loop robust control scheme with performance separation: Theory and experimental validation," *IEEE Transactions on Industrial Electronics*, vol. 69, no. 12, pp. 13483–13493, 2022.

[46] L. M. NXT, "Lego mindstorms nxt," 2004.